A bespoke microfluidic pharmacokinetic compartment model for drug absorption using artificial cell membranes

Jaime L. Korner, Elanna B. Stephenson and Katherine S. Elvira

2020

This article was originally published at:
https://doi.org/10.1039/d0lc00263a

Article correction published at: https://doi.org/10.1039/d0lc90071k

---

Citation for this paper:

Korner, J. L., Stephenson, E. B., & Elvira, K. S. (2020). Correction: A bespoke microfluidic pharmacokinetic compartment model for drug absorption using artificial cell membranes. *Lab on a Chip,* 20(11). https://doi.org/10.1039/d0lc00263a

Lab on a Chip

ROYAL SOCIETY OF CHEMISTRY

PAPER

View Article Online
View Journal | View Issue

Check for updates

Cite this: *Lab Chip*, 2020, **20**, 1898

Received 13th March 2020,
Accepted 4th April 2020

DOI: 10.1039/d0lc00263a

rsc.li/loc

A bespoke microfluidic pharmacokinetic compartment model for drug absorption using artificial cell membranes†

Jaime L. Korner, ‡ Elanna B. Stephenson ‡ and Katherine S. Elvira *

Early prediction of the rate and extent of intestinal absorption is vital for the efficient development of orally administered drugs. Here we show a new type of pharmacokinetic compartment model that shows a threefold improvement in the prediction of molecular absorption in the jejunum than the current state-of-the-art *in vitro* technique, parallel artificial membrane permeability assays (PAMPA). Our three-stage pharmacokinetic compartment model uses microfluidic droplets and bespoke, biomimetic artificial cells to model the path of a drug proxy from the intestinal space into the blood *via* an enterocyte. Each droplet models the buffer and salt composition of each pharmacokinetic compartment. The artificial cell membranes are made from the major components of human intestinal cell membranes (L-α-phosphatidylcholine, PC and L-α-phosphatidylethanolamine, PE) and sizes are comparable to human cells (∼0.5 nL). We demonstrate the use of the microfluidic platform to quantify common pharmacokinetic parameters such as half-life, flux and the apparent permeability coefficient (P_{app}). Our determined P_{app} more closely resembles that of actual intestinal tissue than PAMPA, which overestimates it by a factor of 20.

1 Introduction

In this paper, we present a new method for the *in vitro* quantification of passive drug diffusion. We have developed a microfluidic platform to create a new type of pharmacokinetic compartment model using artificial cell membranes created from a phospholipid mixture designed to mimic human cells. The measurement and prediction of pharmacologically relevant processes such as intestinal absorption are key to successful and efficient drug development.[1,2] New drugs take on average 10–15 years[3] to be developed and cost around 2.6 billion US dollars each.[4] Around 30% of drug candidates fail during testing on animals because we cannot accurately predict their pharmacokinetics.[5,6] Current methods used to predict passive drug transport have limitations including biological dissimilarity, high time and labour input, and lack of control over assay composition.[7–11] We have developed a "slow microfluidic" platform that uses droplets covered in bespoke phospholipid mixtures to form artificial cell membranes that mimic the pathway that drugs follow from the intestine into blood *via* an enterocyte.

At present, oral drug absorption is predicted using a variety of *in vitro* methods that range in complexity from cell-based assays to artificial membrane models.[1,2] Drug absorption can occur through both carrier-mediated uptake and passive lipoidal diffusion.[12] With cell-based techniques, the estimation of drug transport through both passive diffusion and carrier-mediated transport can be simultaneous, using supported monolayers of standard cell lines such as Caco-2 or Madin–Darby canine kidney (MDCK) to model transport out of the small intestine.[13,14] Data gathered from these assays are used to calculate apparent permeability coefficients (P_{app}) which correlate to *in vivo* fractional drug absorption (F). These cell lines are also able to mimic the physiological properties of enterocytes such as microvilli.[15] Conversely, artificial membrane models, such as liposome-based assays and parallel artificial membrane permeability assays (PAMPA), have other advantages: relatively low labour requirements, the ability to isolate the role of lipoidal diffusion, and tunability, which allows the mimicking of different types of membranes.

Liposomes can be comprised of one[20] or more[21] phospholipids, or even sourced directly from living cell membranes.[22] Results from these assays correlate well with human intestinal absorption in some cases.[20] However,

---

Department of Chemistry, University of Victoria, Victoria, BC, Canada. E-mail: kelvira@uvic.ca; Tel: +1 250 721 7165

† Electronic supplementary information (ESI) available: Control experiments, fluorescence intensity measurements, calibration curves, artificial cell membrane surface area calculations, droplet volume calculations, details about the heating platform, mask design and video of the device in operation. See DOI: 10.1039/d0lc00263a

‡ These authors contributed equally to this work.

liposome-based predictions of drug absorption rely on the use of bulk solutions, eliminating the potential for the creation of tunable, biomimetic pharmacokinetic compartments. Therefore we focus on the comparison of our model to PAMPA. There is no research to show that the membranes formed in PAMPA resemble true phospholipid bilayers as found in cells. In PAMPA, *in situ* drug absorption occurs through phospholipid-doped plastic filters placed in 96 well plates.[16] The lipid composition can be customised, and the pH in the donor and acceptor compartments on either side of the filter can be tuned to mimic physiological conditions in specific tissues, which is a vital parameter in assessing the transport of ionisable compounds.[17] Concerns have been raised regarding the disproportionate thickness of the plastic filter used (~125 μm)[18] in comparison to the thickness of a cell membrane (~5 nm)[19] as well as the presence of organic solvent in the interior of the phospholipid "membrane".[18]

Our artificial cell membranes are based on droplet interface bilayers (DIBs), which are lipid bilayers created by bringing two aqueous droplets covered by lipid monolayers into contact (Fig. 1). Since they were first created,[23,24] DIBs have almost exclusively been made with the archaeal phospholipid 1,2-diphytanoyl-*sn*-glycero-3-phosphocholine (DPhPC), with a handful of exceptions, including soy[25] and *E. coli*[26] total lipid extracts. Here we show the first example of DIBs with human-mimicking phospholipid compositions.

Many different methods for the formation of DIBs using microfluidic technologies[27,28] have been developed since we published the first high-throughput method in 2010.[29] Lipid bilayers can also be formed in chambers in microfluidic platforms.[30–32] However, these methods cannot form multiple compartments of cell-scale droplets using human-mimetic phospholipid compositions in high-throughput. Therefore we have designed a new channel-based droplet microfluidic technology where a high level of control over fluid flow rates and droplet position are prioritised. To enable the prediction of pharmacologically relevant drug absorption in this *in vitro* platform, there are three design constraints. Firstly, the platform must be capable of forming droplet triplets of three different compositions, ABC, where A, B and C denote the different compartments in the pharmacokinetic model. Secondly, each droplet should be cell-scale and formed in high-throughput with high reproducibility. And finally, the platform design and surrounding equipment should be simple, to enable replication in other laboratories.

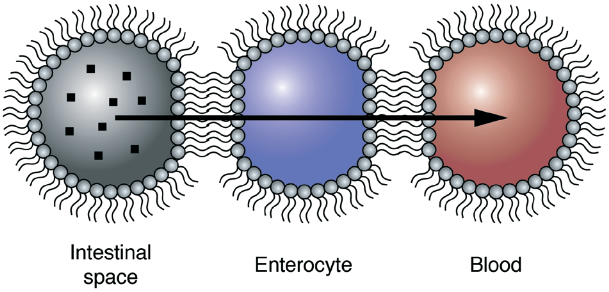

Fig. 1 A new type of pharmacokinetic compartment model. Our *in vitro* droplet-based pharmacokinetic compartment model is designed to mimic the path that an orally administered drug follows from the intestine to the blood. Each compartment is made from a ~0.5 nL microfluidic droplet, where the interior of the droplet represents the compartment itself, and the phospholipid bilayer between the droplets represents an artificial cell membrane. The first droplet (droplet A, grey) mimics the intestinal space, the second droplet (droplet B, purple) mimics an enterocyte and the third droplet (droplet C, red) mimics the blood. Diffusion of a fluorophore (represented in the intestinal space droplet as black squares) occurs in the direction of the arrow.

In our platform (Fig. 2), three different types of ~0.5 nL droplets are created and brought into contact with each other to form DIBs using rails in parallel at a rate of 0.5 Hz. Rails were first used for guiding droplet movement in series in microfluidic devices by Abbyad *et al.*[33] and for DIB formation by Carreras *et al.*, who use the rails to direct droplets for the formation of AB chains of DIBs in series.[34] In comparison, the novel use of three parallel rails allows us to control the flow of droplets into triplet DIB networks and has the potential to allow parallel assays to be performed in the same on-chip structure. Once a triplet is formed, we use a pressure pump to instantly stop the flow for assay quantification without the need for any other on-chip features such as pillars[35] or electromagnetic valves.[36] For comparison, Czekalska *et al.*[36] were able to form one DIB ABCD network at a time and hold it in place for measurements using droplets that were approximately 500 nL in size at a rate of approximately one per minute. Also noteworthy is the microfluidic platform developed by Schmidt *et al.*[35] using approximately 5 nL AB droplets in series and the synthetic lipid 1,2-dioleoyl-*sn*-glycero-3-phosphocholine (DOPC) to measure the permeability of caffeine. Schmidt *et al.* do not report a formation rate and their platform relies on pillars and manually activated oil-withdrawing channels to form DIBs, which limits the potential for automation and increased throughput. The DIBs themselves are formed using a formulation composed of a single (synthetic) phospholipid, whereas cell membranes are usually formed of a formulation of many different types of phospholipids.[37] Other microfluidic platforms for the formation of DIBs are also flow-based, but only able to form networks of ABAB configuration.[29,38] Our platform allows us to form multiple pharmacokinetic assays simultaneously using only a pressure pump with a fast response time and one pressure channel per droplet type.

We have used our microfluidic platform to create a droplet triplet that mimics the path that an orally administered drug follows from the intestine to the blood (Fig. 1), with droplet A mimicking the intestinal space, droplet B mimicking an enterocyte and droplet C mimicking the blood. Pharmacokinetic compartment models describe tissues as mathematical compartments, simplifying the prediction of the distribution of drugs in the body. A single-compartment model treats the body as a single space, assuming that the administered drug is uniformly distributed, while a multicompartmental model integrates tissue-specific rates of absorption and distribution into these calculations.[39] Here

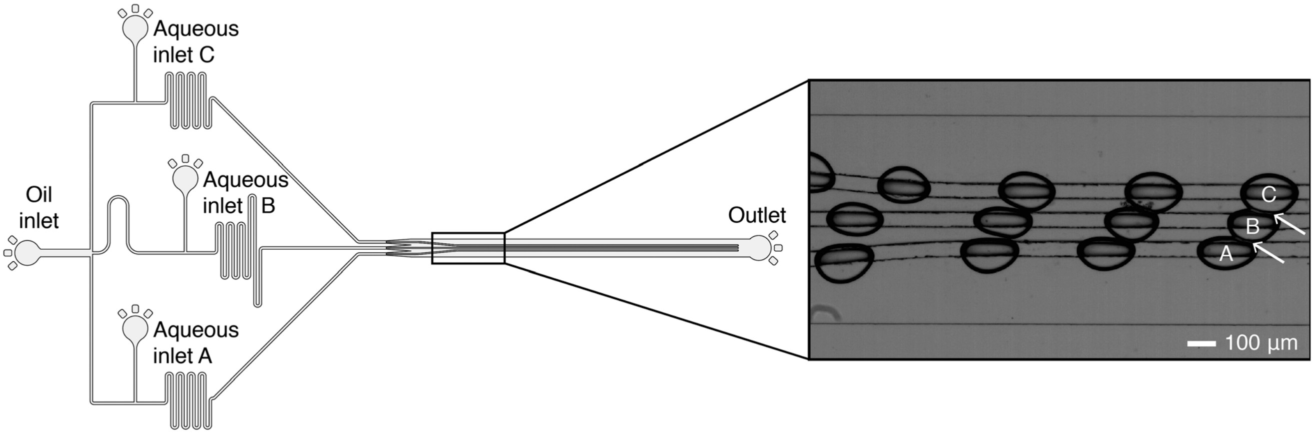

Fig. 2 Microfluidic platform. Design of the "slow microfluidic" platform for the formation of ABC droplet triplets. The device schematic shows the three separately controlled aqueous inlets (A, B and C) used for the formation of three different aqueous droplets at three T-junctions. Each droplet represents a compartment in the pharmacokinetic model. To equilibrate the pressure in the system, a single oil inlet is used and the length of each channel is the same before and after each T-junction. Stabilisation of the lipid monolayer covered aqueous droplets occurs as they travel through the meanders, and bilayer formation occurs when the rails guide the droplets into contact with each other. Each DIB represents an artificial cell membrane between each compartment. The inset is a photograph showing the formation of ABC DIB triplets in parallel using the rails. The continuous phase is squalene and aqueous droplets contain 10 mM HEPES, 140 mM KCl and 10 mg mL^{-1} DPhPC at pH 6.5. Arrows highlight the artificial cell membranes formed between the droplets. A video of the microfluidic platform in use is provided in the ESI.†

we present a new type of pharmacokinetic compartment model, using droplets to model human tissues which are relevant to the absorption of orally administered drugs while maintaining important properties such as pH, ionic strength and phospholipid composition. The interior of each droplet is a buffer (Table 1) that mimics the pH and salt composition of each these compartments[40–42] and the artificial cell membrane between each droplet is an equal mixture of the phospholipids L-α-phosphatidylcholine (PC) and L-α-phosphatidylethanolamine (PE), a pared down version of the lipid formulation used in PAMPA assays to mimic the small intestine,[43] since these are the major components of intestinal cell membranes.[44–50] The droplet size mimics the volume of human cells[51] and is within two orders of magnitude of the size of human enterocytes.[52–54] Most importantly, the size of droplets formed is ten times smaller than the smallest droplets used in the literature for DIB diffusion quantification.[35] This microfluidic platform allows the quantification of the passive diffusion of fluorescein, which is commonly used as a drug proxy in release studies,[55–58] from the intestinal compartment to the blood compartment. Our new *in vitro* technique for the quantification of drug absorption of orally administered drugs provides an alternative to PAMPA for the determination of fluorescent drug absorption rates. Our method preserves the compartment model seen in PAMPA, but replaces the thick, lipid-filled membrane with a biomimetic lipid mixture that mimics that found in human cells. We also preserve the differing rates of diffusion seen with different ionisation states of a drug in the gastrointestinal tract.

Table 1 Composition of the buffers used for each pharmacokinetic compartment

Droplet designation	Buffer	Salt
Intestinal space[40,59]	10 mM Na_2HPO_4, pH 6.5	140 mM KCl
Enterocyte	10 mM HEPES, pH 7.4	140 mM KCl
Blood[60]	10 mM Na_2CO_3, pH 7.4	140 mM NaCl

2 Materials and methods

2.1 Materials

1,2-Diphytanoyl-*sn*-glycero-3-phosphocholine (DPhPC, ≥99% pure) was purchased from Avanti Polar Lipids. Sodium phosphate dibasic and sodium phosphate monobasic were purchased from Fisher Scientific. Sodium chloride and sodium carbonate were purchased from Bio Basic. L-α-Phosphatidylcholine (PC, ≥99% pure, bovine liver), L-α-phosphatidylethanolamine (PE, ≥97% pure, bovine liver), squalene (≥98% pure), 4-(2-hydroxyethyl)-1-piperazineethanesulfonic acid (HEPES, ≥99.5% pure), trimethylchlorosilane (≥99% pure), sodium fluorescein (BioReagent, suitable for fluorescence), potassium hydroxide, hydrochloric acid (≥36.5–38%) and potassium chloride (≥99% pure) were purchased from Millipore Sigma. Polydimethylsiloxane (PDMS, Dow Sylgard 184) was purchased from Ellsworth Adhesives. Acetate masks were printed at 10 μm resolution by CAD/Art Services Inc. Silicon wafers (100 mm diameter) were purchased from Silicon Materials. SU-8 3050 and developer were purchased from MicroChem. Polytetrafluoroethylene (PTFE, 1/16″ outer diameter, 250 μm inner diameter) tubing was purchased from Chromatographic Specialties Inc.

2.2 Design and fabrication of the microfluidic platform

Microfluidic devices (Fig. 2) have two layers. The first layer contains the channels and geometries used for the formation of the three different types of droplets used to model each pharmacokinetic compartment. The second layer contains the rails, which are 50 μm apart. The three rails encourage the three aqueous droplets covered with a phospholipid monolayer to come into contact to form an artificial cell membrane at the points of interaction. The 5° angle of the rails means that the droplets can be brought into contact at a slow speed of approximately 40 μm s^{-1}. The layers were designed using AutoCAD (Autodesk, 2018, see ESI†) and printed onto acetate to create positive photomasks. A 50 ± 2 μm layer of the negative photoresist SU-8 3050 was spin-coated onto a silicon wafer, and the edgebead was removed with a stream of acetone. The wafer was subjected to a soft bake (5 min at 35 °C, 2 min at 65 °C and 30 min at 95 °C), and subsequently exposed to UV light (11.2 s, 19.96 mW cm^{-2}, OAI Model 800 mask aligner) through the first photomask. A second layer was spin-coated, soft baked, aligned and exposed to UV using the same parameters and the second layer photomask. Development removed the unexposed, non-crosslinked SU-8, and adhesion of the SU-8 features was accelerated by a final hard bake (30 min at 200 °C) and a third UV exposure (90 s, 19.96 mW cm^{-2}).

Trimethylchlorosilane (50 μL) and the wafer mould were placed under vacuum for 1 h to ensure the deposition of a thin film of silane on the surface of the wafer. PDMS base and curing agent were mixed together in a 10 : 1 ratio, poured over the aforementioned mould, degassed for 1 h under vacuum to remove any air bubbles introduced during mixing, and cured overnight at 65 °C. The cured PDMS was then peeled from the mould. Inlets and outlets for each device were punched using a 1 mm biopsy punch. To create the base of the device, a 10 : 1 mixture of PDMS base and curing agent was mixed, degassed and spincoated at 1200 rpm for 25 s onto the surface of glass microscope slides to create a thin layer. Both the PDMS devices and the coated glass slides were washed with soapy reverse osmosis (RO) water, rinsed with RO water, isopropyl alcohol, ethanol and Milli-Q water, blown dry with filtered air, baked at 90 °C for 30 min, treated with air plasma (Diener Electronic, Zepto ONE, 37 s, 29 W, 1.75 mbar) to activate the surfaces and placed into contact with each other to bond the surfaces together. The microfluidic devices were then stored at 65 °C for a minimum of 48 h prior to use.

2.3 Preparation of lipid solutions

Chloroform was removed from the lipid stock solutions by placing 10 mg (400 μL of a 25 mg mL^{-1} solution dispensed using a P1000 Gilson pipette) of lipids in a 10 mL glass roundbottom flask, and rotating the flask under a stream of nitrogen gas to create a thin film. The flask was then placed in a desiccator under vacuum for 1 h to remove residual solvent. For DPhPC solutions, 1 mL aqueous buffer (buffer composition is the same as that of the intestinal space in Table 1) was then added and the flask was vortexed to resuspend the lipids. After freezing and thawing 5 times using liquid nitrogen and warm water, the lipids were extruded 21 times through a 0.1 μm polycarbonate membrane (Avanti Polar Lipids) at room temperature. For 1 : 1 PC : PE solutions, 1 mL of squalene was added to the flask, which was then vortexed for 30 s and stirred at 50 °C until the phospholipids dissolved. The final concentration was 5 mg mL^{-1} PC and 5 mg mL^{-1} PE in squalene. For absorption experiments, 100 μM fluorescein sodium was added to the buffer.

2.4 Operating parameters of the microfluidic platform

For all experiments, devices were mounted in a custom-made heating platform set to 37 °C (see the ESI† for further details) on the stage of either a Nikon Eclipse Ti2-E or a Nikon Eclipse Ti2-U inverted microscope for visualisation. Brightfield images for statistical analysis were collected using a Motion Blitz EoSens Cube7 or a Phantom VEO 710L high speed camera. Fluorescence and brightfield images for fluorescence experiments were captured using a Hamamatsu ORCA-Flash4.0 V3, with a Solis-1C cold white LED (Thorlabs) and a GFP Semrock Brightline large field of view filter cube (Nikon).

Reagents were introduced into the microfluidic devices using an Elveflow OB1 MK3 pressure pump, four 1.5 mL Eppendorf tubes as reservoirs and four matched lengths of PTFE tubing. Squalene and aqueous buffers were introduced to the microfluidic device by applying a pressure of 100 mbar to 140 mbar to the squalene reservoir, and a pressure of 60 mbar to 100 mbar to each of the aqueous reservoirs. Following equilibration, the main chamber was monitored in Motion Blitz Director for quantification of device performance, and NIS Elements Advanced Research (Nikon, version 5.11.01) for fluorescence data collection. Following formation of a triplet for a fluorescence experiment, flow was stopped from all reservoirs from within the Elveflow control software. Typical droplet speeds were approximately 450 μm s^{-1}, allowing this full stop to be done without the use of triggers.

The speed at which droplets are brought into contact with each other is crucial for the formation of stable artificial cell membranes, and this is especially true when using phospholipids below their phase transition temperatures, as we do here. The response time of the pressure pump means that the flow can be stopped within 130 ms of when an ABC droplet triplet forms and the assay starts. We are therefore able to accurately determine the initial time point of the assay and to discard substandard triplets.

2.5 Fluorescence data collection

Once ABC droplet triplets formed and the flow was stopped, brightfield and fluorescence images were taken every 10 s with a 300 ms exposure time until experiment termination. Quantification of fluorescence intensity was performed *via* time-based measurement of mean intensity in regions of interest (ROIs) within each droplet in each frame using NIS Elements. Fluorescence intensity data was normalised for phospholipid bilayer surface area and droplet volume. To do this, bilayer diameters and droplet semiaxes were measured using, respectively, the “Distance Measurement” and the “Measurements and Annotations” modules in NIS Elements.

Subsequent calculations were performed by approximating artificial cell membrane surface area as ellipses and droplet volumes as ellipsoids. Each graph in this paper represents the replicate of 5 experiments conducted on 5 different microfluidic devices. Fig. S2–S3 in the ESI† provide detailed information about the ROI selection, the quantification of fluorescence intensity, volume calculations and data normalisation for the artificial cell membrane surface area and droplet volume.

2.6 Quantification of microfluidic device performance

To quantify the performance of the microfluidic devices, squalene was pumped into the oil inlet and DPhPC in buffer was pumped into each of the three aqueous inlets with the pressure pump in constant pressure mode. Assessment of the efficacy of ABC DIB triplet formation on the platform was performed using DPhPC to allow for comparison with other DIB forming methodologies in the literature. After letting the flow equilibrate, the high-speed camera was centered on the main chamber, and 60 s of footage were captured for each replicate. The number of ABC DIB triplets formed in each sequence was counted, as summarised in Table 2. The total number of droplets forming triplets was then determined as a percentage of the total number of droplets passing through the field of view. To show the robustness of our method, two sets of two replicates each were carried out, with a different researcher carrying out each set on separate days. For each replicate, a different microfluidic device was used. Statistical analysis indicated that triplets could be formed at a rate of 0.5 ± 0.1 Hz and that 45 ± 8% of droplets entering the rail section of the platform were able to form triplets. No precedent for reproducibility exists in the literature, so these data may serve as a benchmark by which throughput and reproducibility of DIB-forming methodologies (both microfluidic and not) may be assessed.

3 Results and discussion

3.1 A new *in vitro* model for intestinal absorption

The time-resolved diffusion of fluorophore between pharmacokinetic compartments A, B and C may be seen in Fig. 3. Timepoints are chosen to show when the fluorophore is concentrated in the intestinal compartment A (t = 0 s), a mid-assay timepoint (t = 420 s) where the fluorophore is concentrated in the enterocyte compartment B, and the endpoint of the assay (t = 1800 s). All data were gathered at physiological temperatures (37 °C).

Fig. 4 shows the change in fluorophore concentration over time for each compartment in the system. Given the well-known nature of PDMS and its effect on droplet behaviour,[61] intensity measurements were first scaled based on changes in droplet volume over the course of the experiment, due to

Table 2 Statistical data used to quantify device performance. All replicates were collected from 60 s of video captured at 30 frames per second. Triplets were counted from the beginning of the captured video and the number of triplets (n) for each experimental repeat are shown in the first column

n	Formation rate	Oil pressure	Aqueous pressure
34	0.57 Hz	120 mbar	113 mbar to 115 mbar
32	0.53 Hz	120 mbar	113 mbar to 115 mbar
26	0.43 Hz	100 mbar	90 mbar to 95 mbar
18	0.30 Hz	100 mbar	90 mbar to 95 mbar

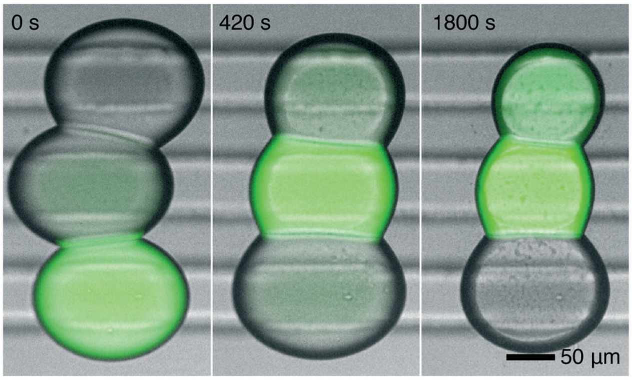

Fig. 3 Images of fluorophore diffusion. Composite brightfield and fluorescence images showing the diffusion of fluorophore from the droplet that represents the intestinal space in the pharmacokinetic compartment model (t = 0 s, bottom, droplet A), to the droplet that represents an enterocyte (t = 420 s, middle, droplet B), after which it continues diffusing into the droplet that represents blood (t = 1800 s, top, droplet C). The fluorophore in the fluorescence images has been tinted green to aid visualisation. Brightfield and colour intensity-corrected fluorescence images were exported from NIS Elements and overlaid with a screen blending mode. Brightness was raised to visible levels by applying a lookup table.

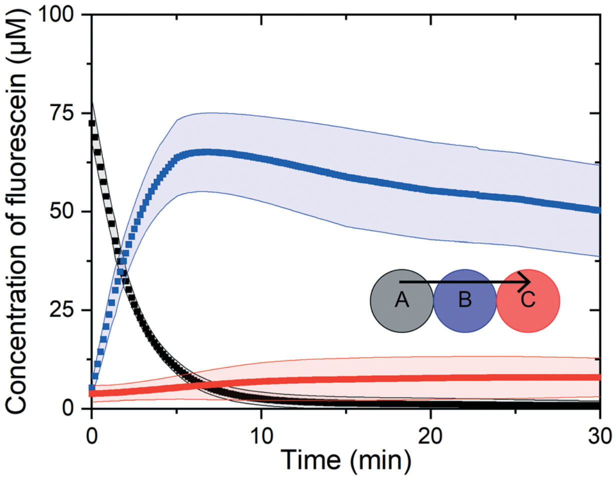

Fig. 4 Fluorophore diffusion over time. Normalised concentration curves for each pharmacokinetic compartment in the droplet triplet model over 30 minutes. The fluorophore is initially concentrated in the droplet representing the intestinal space, A, but rapidly diffuses through the artificial cell membrane into the droplet representing an enterocyte, B, and slowly diffuses through the artificial cell membrane into the droplet representing the blood, C. 95% confidence bands were calculated from the standard deviation for each timepoint, where n = 5 using 5 different microfluidic devices.

either evaporation or osmosis, using eqn (1), where I_s is the scaled intensity, I_t is the intensity at time t, and V_t and V_0 are the droplet volumes at times t and 0 respectively. To determine concentration and account for pH-dependent changes in fluorophore intensity, calibration curves were generated for fluorescein in each buffer and a linear fit was calculated using OriginPro 2019b. Concentration was then calculated from the fitted curve using the scaled intensity measurements. Calibration curves (Fig. S4–S6†) and additional experimental information are provided in the ESI.†

$$I_s = I_t \frac{V_t}{V_0} \tag{1}$$

Fig. 5 shows the absorption of the fluorophore from the intestinal space compartment A into the enterocyte and blood compartments, B and C. The rapid absorption of the fluorophore from the intestinal space into both the enterocyte and the blood can be clearly seen. To find the half-life $\left(t_{\frac{1}{2}}\right)$ of the fluorophore in the intestinal space, an exponential curve of the form $y = a - bc^x$ was fitted to these data in OriginPro. This curve fitting found the parameters $a = 0.976 \pm 0.001$, $b = 1.004 \pm 0.007$, and $c = 0.99311 \pm 0.00005$. The slope of the intensity curve gives the diffusion rate. From this curve a $t_{\frac{1}{2}}$ of 108 ± 2 s was determined.

The accuracy of this technique was improved by accounting for the area dependence of diffusion rates through the artificial cell membrane. This flux was calculated using eqn (2), where j_t is the flux at time t, $\Delta C/\Delta t$ is the momentary slope (C is concentration), and $A_{\mathrm{DIB},t}$ is the measured artificial cell membrane area at time t.

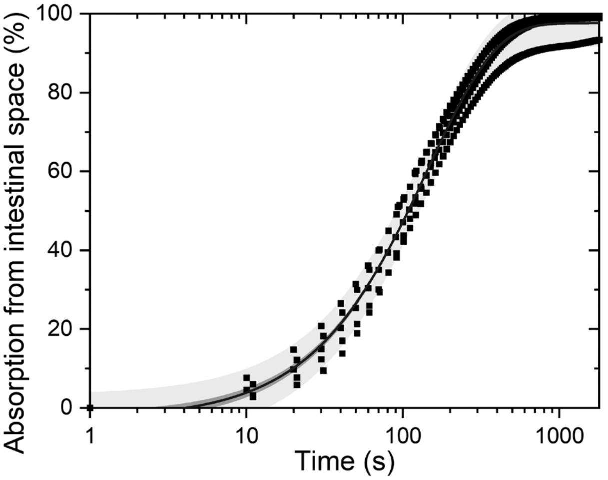

Fig. 5 Fluorophore absorption over time. Absorption of fluorophore from the intestinal space compartment A, into the enterocyte compartment, B, shown as the percentage of fluorescence decrease from initial intensity. The fitted curve and narrow confidence band allow the prediction of the half-life of the fluorophore in the intestinal space compartment with a 2% relative standard deviation.

$$j_t = \frac{\Delta C}{\Delta t} \frac{1}{A_{\mathrm{DIB},t}} \tag{2}$$

The flux of all five runs is plotted in Fig. 6. Following curve fitting the y-intercept, $j_{\max}$, was calculated to be −0.117 ± 0.002 nM s^{-1} $\mu\mathrm{m}^{-2}$.

3.2 Correlation to cell-based assays

Our method is three times better at predicting P_{app} of actual intestinal tissue than PAMPA. For direct comparison with literature permeability values for fluorescein, we adapted the equation for the P_{app} used by Berginc *et al.*[62] We treated the system as a two-compartment model, allowing us to treat diffusion out of the intestinal space (droplet A) as having the same magnitude as diffusion into the enterocyte (droplet B). This gives eqn (3), where $\Delta C/\Delta t$ ($\mu\mathrm{M\ s}^{-1}$) is the maximum rate of diffusion out of droplet A, V (cm^3) is the initial volume of droplet B, C_0 (μM) is the initial concentration of droplet A, and A (cm^2) is the maximum artificial cell membrane surface area.

$$P_{\mathrm{app}} = \frac{-\Delta C_{\max}}{\Delta t} \frac{V}{C_0 A} \tag{3}$$

We found P_{app} to be $5.6 \pm 0.7 \times 10^{-5}$ cm s^{-1}. PAMPA assays carried out previously by Berginc *et al.*[62] found P_{app} for fluorescein to be $16 \pm 3 \times 10^{5}$ cm s^{-1} with pH 6.5 and 7.5 in the donor and acceptor compartments respectively, which is a whole order of magnitude higher than our value. However when they performed this absorption assay using rat jejunum under the same pH conditions we used they found P_{app} to be $0.8 \pm 0.1 \times 10^{5}$ cm s^{-1}.

3.3 Control experiments

Direct comparison of the fluorophore intensity between the compartments is complicated by matrix differences since the

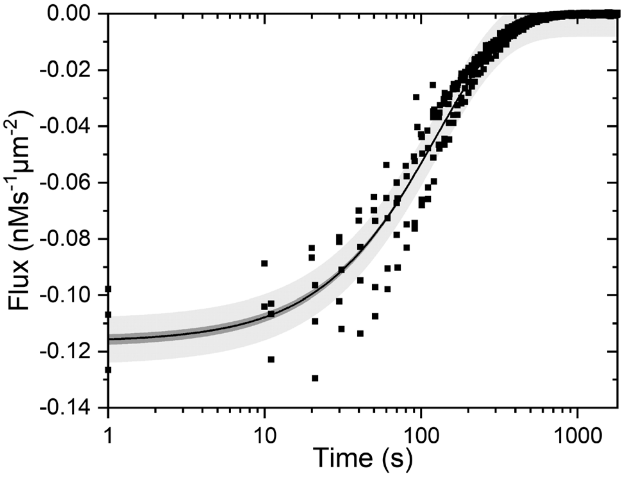

Fig. 6 Fluorophore flux over time. Flux of fluorophore from the intestinal space compartment, A, into the enterocyte, B, calculated using eqn (2). Maximum flux may be determined using the fitted curve, providing a measurement of the permeability of the artificial cell membrane to the fluorophore.

composition of the droplets was customised to mimic specific biological compartments using different buffering agents and salts. Interestingly, there was a very narrow spread of data for the fluorophore leaving the intestinal space compartment (droplet A), but a wider spread of behaviours upon entering the enterocyte and blood droplets (droplets B and C). This can be seen as a wider spread in Fig. 4 for these compartments. Control experiments were performed to assess the matrix effect, which was easily done with this microfluidic platform. In these control experiments, the fluorophore was always dosed in droplet A (the intestinal space), but the composition of the triplet was varied to allow a different diffusion pathway in each case, namely: AAA, BAC, ABB, ACC and ACB, where B represents an enterocyte and C represents the blood (see Fig. S7 in the ESI† for data).

As expected, complete fluorophore equilibration was observed when all three compartments were tuned to mimic the pH and ionic composition of the intestinal space (AAA). Likewise, when triplets of the composition BAC were formed, rapid equivalent diffusion out of droplet A into droplets B and C was observed, and in the case of ABB triplets, rapid diffusion into the first B droplet, B_1, was followed by equilibration between both B droplets. The behavior of ACB triplets closely followed that of ABC triplets. However, when ACC triplets were formed, rapid diffusion into C_1 occurred, and the fluorophore did not continue into the second C droplet, C_2. In all cases where pH 7.4 droplets were tested with pH 6.5 droplets, fluorescein demonstrated a clear preference for pH 7.4 compartments.

The primary driving force for the selective diffusion path seen in our pharmacokinetic compartment model is the different pH environments encapsulated in droplets A and B, and hence the fluorophore rapidly leaves the intestinal space and enters the enterocyte. Fluorescein has a pK_a at 6.43,[63] so a larger fraction of molecules exist in the less lipid-soluble dianionic form at pH 7.4 and a larger fraction exist in the more lipid-soluble monoanionic form at pH 6.5. This effectively allows fluorescein to easily diffuse into the artificial cell membrane from the intestinal space, but to diffuse back into the intestinal space from the enterocyte at a far reduced rate. This ties rate of diffusion to lipophilicity in the same way as PAMPA.[16] The fluorescein monoanion and dianion exhibit slight differences in absorption and emission spectra, including in fluorescence intensity and quantum yield,[64,65] which is accounted for using calibration curves as described above and in Fig. S4–S6 in the ESI.† The movement of the fluorophore between droplets B and C, which are at the same pH, is explained by the second driving force for the observed transport phenomenon, which is the difference in osmolality between these droplets.[66]

$$\text{Osmolality} = 2[\text{Na}^+ + \text{K}^+] + [\text{urea}] + [\text{glucose}] \quad (4)$$

Respectively, the calculated osmolalities of droplets A, B, and C are 320 mM, 280 mM, and 320 mM. Diffusion will be driven towards higher osmolality compartments, but because the majority of fluorescein exists as a dianion in droplet B and thus cannot diffuse back into droplet A, the equilibrium lies further towards droplet C.

4 Conclusions

Here we show a new type of pharmacokinetic compartment model with higher correlation to cell-based assays than PAMPA, the current state-of-the-art technology. This suggests that a higher degree of *in vitro–in vivo* correlation may also be found using our bespoke pharmacokinetic compartment model. We intend our method to be complementary to cell-based assays by providing a way of creating bespoke artificial cell membranes and pharmacokinetic compartments to quantify the effect that each component has on drug transport.

We have used a new type of microfluidic platform for the formation of DIBs in parallel to build a pharmacokinetic compartment model of the path that an orally administered drug takes from the intestinal space, into enterocytes, and finally into the blood. We demonstrate how this compartment model can predict pharmacokinetic properties of a drug including half-life, flux and P_{app}. Our pharmacokinetic compartment model demonstrates a greater degree of similarity of P_{app} to a true biological system (rat jejunum) than is possible with PAMPA.

Our microfluidic platform is simple to use (it only requires a fast response pressure pump) and allows bespoke artificial cells to be formed of sizes (~0.5 nL) that more closely mimic human cells than preceding work using the major phospholipid components (PE and PC) of intestinal cells. We demonstrate and quantify the reproducibility of this platform and show the collection of data with far better time resolution than previously possible. Ongoing and future developments include modeling drug transport in other human tissues and investigating new drug tagging and detection methods.

The limited correlation between *in vitro* and *in vivo* methods for the prediction of drug behaviour in humans is a severe constraint in the timely and cost-effective development of new drugs. Our new *in vitro* model could allow the early prediction of pharmacokinetic parameters of drug candidates by enabling researchers in academia and the pharmaceutical industry to build bespoke pharmacokinetic compartment models.

Contributions

EBS designed and developed the microfluidic device for the formation of ABC droplet triplets. JLK developed the biomimetic lipid formulations for use in the microfluidic platform. EBS and JLK conducted the triplet formation experiments for the quantification of device performance and gathered preliminary data for the fluorescence diffusion experiments in duplicate. JLK collected the fluorescence diffusion data we present in this paper. EBS collected the data for the calibration curves. EBS and JLK performed half the control experiments each. JLK performed the volume and surface area measurements, and the measurements of ROI and intensity. EBS performed the data normalisation and data analysis. KSE designed the concept of building bespoke human-mimetic artificial cell membranes in this manner as a new type of pharmacological compartment model, supervised EBS, JLK, and AEM, and guided all experimental decisions. EBS, JLK and KSE wrote the paper.

Conflicts of interest

There are no conflicts to declare.

Acknowledgements

This research was funded through the Natural Sciences and Engineering Research Council of Canada (NSERC) Discovery Grant program. Dr. Elvira's position is funded through the Canada Research Chair program and her laboratory was equipped using funding from the Canada Foundation for Innovation John R. Evans Leaders Fund (CFI-JELF), the British Columbia Knowledge Development Fund (BCKDF) and the NSERC Research Tools and Instruments program. We also acknowledge Alberto Escobar Mingo for building the heating platform used in this work, and for writing the ESI† section detailing its performance.

References

1 T. A. Baillie, *Chem. Res. Toxicol.*, 2008, **21**, 129–137.

2 T. D. Y. Chung, D. B. Terry and L. H. Smith, *In vitro and in vivo assessment of ADME and PK properties during lead selection and lead optimization – Guidelines, benchmarks and rules of thumb*, Eli Lilly & Company and the National Center for Advancing Translational Sciences, Bethesda (MD), 2015.

3 Institute of Medicine (US) Committee on Conflict of Interest in Medical Research, Education, and Practice, *Conflict of interest in medical research, education, and practice*, National Academies Press (US), Washington (DC), 2009.

4 J. A. DiMasi, H. G. Grabowski and R. W. Hansen, *J. Health Econ.*, 2016, **47**, 20–33.

5 A. Avdeef, *Curr. Top. Med. Chem.*, 2001, **1**, 277–351.

6 M. Ceccarelli, B. Wagner, R. Alvarez-Sánchez, G. Cruciani and L. Goracci, *Chem. Res. Toxicol.*, 2017, **30**, 1145–1156.

7 H. Sun, E. C. Chow, S. Liu, Y. Du and K. S. Pang, *Expert Opin. Drug Metab. Toxicol.*, 2008, **4**, 395–411.

8 P. V. Balimane and S. Chong, *Drug Discovery Today*, 2005, **10**, 335–343.

9 A. Avdeef, S. Bendels, L. Di, B. Faller, M. Kansy, K. Sugano and Y. Yamauchi, *J. Pharm. Sci.*, 2007, **96**, 2893–2909.

10 S. Alqahtani, L. A. Mohamed and A. Kaddoumi, *Expert Opin. Drug Metab. Toxicol.*, 2013, **9**, 1241–1254.

11 F. Nigsch, W. Klaffke and S. Miret, *Expert Opin. Drug Metab. Toxicol.*, 2007, **3**, 545–556.

12 D. Smith, P. Artursson, A. Avdeef, L. Di, G. F. Ecker, B. Faller, J. B. Houston, M. Kansy, E. H. Kerns, S. D. Krämer, H. Lennernäs, H. van de Waterbeemd, K. Sugano and B. Testa, *Mol. Pharmaceutics*, 2014, **11**, 1727–1738.

13 D. A. Volpe, *Future Med. Chem.*, 2011, **3**, 2063–2077.

14 J. D. Irvine, L. Takahashi, K. Lockhart, J. Cheong, J. W. Tolan, H. E. Selick and J. R. Grove, *J. Pharm. Sci.*, 1999, **88**, 28–33.

15 I. J. Hidalgo, T. J. Raub and R. T. Borchardt, *Gastroenterology*, 1989, **96**, 736–749.

16 M. Kansy, F. Senner and K. Gubernator, *J. Med. Chem.*, 1998, **41**, 1007–1010.

17 M. Kataoka, S. Tsuneishi, Y. Maeda, Y. Masaoka, S. Sakuma and S. Yamashita, *Eur. J. Pharm. Biopharm.*, 2014, **88**, 840–846.

18 H. Yu, Q. Wang, Y. Sun, M. Shen, H. Li and Y. Duan, *PLoS One*, 2015, **10**, e0116502.

19 R. C. Warren, *Physics and the architecture of cell membranes*, Hilger, 1987.

20 K. Balon, B. U. Riebesehl and B. W. Müller, *Pharm. Res.*, 1999, **16**, 882–888.

21 S. Purushothaman, J. Cama and U. F. Keyser, *Soft Matter*, 2016, **12**, 2135–2144.

22 I. Osiecka, P. A. Porter, R. T. Borchardt, J. A. Fix and C. R. Gardner, *Pharm. Res.*, 1985, **2**, 284–293.

23 K. Funakoshi, H. Suzuki and S. Takeuchi, *Anal. Chem.*, 2006, **78**, 8169–8174.

24 M. A. Holden, D. Needham and H. Bayley, *J. Am. Chem. Soc.*, 2007, **129**, 8650–8655.

25 N. E. Barlow, E. Smpokou, M. S. Friddin, R. Macey, I. R. Gould, C. Turnbull, A. J. Flemming, N. J. Brooks, O. Ces and L. M. C. Barter, *Biomicrofluidics*, 2017, **11**, 024107.

26 G. J. Taylor and S. A. Sarles, *Langmuir*, 2015, **31**, 325–337.

27 M. A. Czekalska, T. S. Kaminski, K. Makuch and P. Garstecki, *Sens. Actuators, B*, 2019, **286**, 258–265.

28 M.-A. Nguyen, B. Srijanto, C. P. Collier, S. T. Retterer and S. A. Sarles, *Lab Chip*, 2016, **16**, 3576–3588.

29 C. E. Stanley, K. S. Elvira, X. Z. Niu, A. D. Gee, O. Ces, J. B. Edel and A. J. deMello, *Chem. Commun.*, 2010, **46**, 1620–1622.

30 T. Tonooka, K. Sato, T. Osaki, R. Kawano and S. Takeuchi, *Small*, 2014, **10**, 3275–3282.

31 N. Soga, R. Watanabe and H. Noji, *Sci. Rep.*, 2015, **5**, 1–8.

32 M. Urban, A. Kleefen, N. Mukherjee, P. Seelheim, B. Windschiegl, M. Vor der Bruggen, A. Kocer and R. Tampe, *Nano Lett.*, 2014, **14**, 1674–1680.

33 P. Abbyad, R. Dangla, A. Alexandrou and C. N. Baroud, *Lab Chip*, 2011, **11**, 813–821.

34 P. Carreras, Y. Elani, R. V. Law, N. J. Brooks, J. M. Seddon and O. Ces, *Biomicrofluidics*, 2015, **9**, 064121.

35 T. Nisisako, S. A. Portonovo and J. J. Schmidt, *Analyst*, 2013, **138**, 6793–6800.

36 M. A. Czekalska, T. S. Kaminski, M. Horka, S. Jakiela and P. Garstecki, *Micromachines*, 2017, **8**, 93.

37 G. van Meer, D. R. Voelker and G. W. Feigenson, *Nat. Rev. Mol. Cell Biol.*, 2008, **9**, 112–124.

38 B. Schlicht and M. Zagnoni, *Sci. Rep.*, 2015, **5**, 9951.

39 H. M. Jones and K. Rowland Yeo, *CPT: Pharmacometrics Syst. Pharmacol.*, 2013, **2**, 63.

40 E. Stippler, S. Kopp and J. B. Dressman, *Dissolution Technol.*, 2004, **11**, 6–10.

41 F. Lang, *J. Am. Coll. Nutr.*, 2006, **26**, 613S–623S.

42 D. L. Gilbert, *Yale J. Biol. Med.*, 1960, **32**, 378–389.

43 K. Sugano, H. Hamada, M. Machida, H. Ushio, K. Saitoh and K. Terada, *Int. J. Pharm.*, 2001, **228**, 181–188.

44 P. Proulx, *Biochim. Biophys. Acta*, 1991, **1071**, 255–271.

45 G. G. Forstner, K. Tanaka and K. J. Isselbacher, *Biochem. J.*, 1968, **109**, 51–59.

46 S. M. Schwarz, B. Hostetler, S. Ling, M. Mone and J. B. Watkins, *Am. J. Physiol.*, 1985, **248**, G200–G207.

47 T. A. Brasitus, K.-Y. Yeh, P. R. Holt and D. Schachter, *Biochim. Biophys. Acta, Biomembr.*, 1984, **778**, 341–348.

48 K. Christiansen and J. Carlsen, *Biochim. Biophys. Acta, Biomembr.*, 1981, **647**, 188–195.

49 H. Hauser, K. Howell, R. M. C. Dawson and D. E. Bowyer, *Biochim. Biophys. Acta, Biomembr.*, 1980, **602**, 567–577.

50 T. A. Brasitus, N. O. Davidson and D. Schachter, *Biochim. Biophys. Acta, Biomembr.*, 1985, **812**, 460–472.

51 M. B. Ginzberg, R. Kafri and M. Kirschner, *Science*, 2015, **348**, 1245075.

52 R. J. MacLeod, J. R. Hamilton, A. Bateman, D. Belcourt, J. Hu, H. P. Bennett and S. Solomon, *Proc. Natl. Acad. Sci. U. S. A.*, 1991, **88**, 552–556.

53 R. J. Buschmann and D. J. Manke, *J. Ultrastruct. Res.*, 1981, **76**, 1–14.

54 P. T. Crowe and M. N. Marsh, *Virchows Arch. A: Pathol. Anat. Histopathol.*, 1993, **422**, 459–466.

55 S. Stein, M. Bogdahn, C. Rosenbaum, W. Weitschies and A. Seidlitz, *Eur. J. Pharm. Sci.*, 2017, **109**, 233–243.

56 M. E. Khosroshahi and M. Mahmoodi, *Adv. Nanopart.*, 2018, **7**, 720–726.

57 Y. Liu, H. Miyoshi and M. Nakamura, *Colloids Surf., B*, 2007, **58**, 180–187.

58 K. A. Fisher, K. D. Huddersman and M. J. Taylor, *Chem. – Eur. J.*, 2003, **9**, 5873–5878.

59 J. M. Maurer, R. C. A. Schellekens, H. M. van Rieke, C. Wanke, V. Iordanov, F. Stellaard, K. D. Wutzke, G. Dijkstra, M. van der Zee, H. J. Woerdenbag, H. W. Frijlink and J. G. W. Kosterink, *PLoS One*, 2015, **10**, 1–17.

60 T. Kokubo and H. Takadama, *Biomaterials*, 2006, **27**, 2907–2915.

61 A. P. Debon, R. C. R. Wootton and K. S. Elvira, *Biomicrofluidics*, 2015, **9**, 024119.

62 K. Berginc, S. Žakelj, L. Levstik, D. Uršič and A. Kristl, *Eur. J. Pharm. Biopharm.*, 2007, **66**, 281–285.

63 R. Sjöback, J. Nygren and M. Kubista, *Biopolymers*, 1998, **46**, 445–453.

64 M. M. Martin and L. Lindqvist, *J. Lumin.*, 1975, **10**, 381–390.

65 M. J. Doughty, *Ophthalmic Physiol. Opt.*, 2010, **30**, 167–174.

66 L. I. G. Worthley, M. Guerin and R. W. Pain, *Anaesth. Intens. Care*, 1987, **15**, 199–202.